length lens to give a narrow beam of almost constant diameter (0.15 mm approx.) perpendicular to the gas flow. The light scattered perpendicular to the flow, to the incident beam and to the direction of polarization of the beam was collected and collimated by an f1.8 camera lens. This collimated beam passed through a 1 nm band-pass interference filter and was then focused at a slit so as to eliminate stray light before finally being detected by a photomultiplier. The slit also served to determine the length of the sample volume at 0.64 mm. For each experiment the laser power, which was monitored by the photomultiplier, P_T, in Fig. 1, and the gain of the photomultiplier, P_S, were held constant.

The burner assembly consisted of an axisymmetric fuel jet, formed by a quartz nozzle with throat 2.4 mm, and a concentric dust shield, 100-mm-diam, through which a low-velocity airstream was passed. The nozzle was mounted on a settling chamber containing a 50-mm-diam loudspeaker which could be used to impress a small periodic velocity modulation on the jet.[1] Both the fuel (methane) and air flows were filtered using a 25-mm-diam cellulose nitrate filter (pore size, 0.6 μm) to remove dust. This was necessary because the light scattered by a single dust particle can exceed, by more than an order of magnitude, that scattered by all the molecules in the beam. We were able to remove dust particles from the fuel flow completely (less than one particle every 5 min on average) but were less successful with the air supply (approximately one particle every two seconds). However, this latter level was sufficiently low for the purposes of these experiments.

The system was first calibrated by measuring the intensity of the light scattered from pure methane and pure air. The relative proportions (by mole) of methane and air in the sample volume may then be simply obtained by linear interpolation between the pure air and pure methane values. Some fluctuation of the species signals must be expected from photon and photomultiplier noise but secondary contributions also arise from fluctuations in the laser power and possibly from dust particles in the laser beam outside the sample volume. However, since such fluctuations were small in comparison with the concentration-dependent fluctuations no attempt was made to minimize them.

The limiting frequency response, ν_{max} Hz, of the Rayleigh scattering detection system depends on the signal-to-noise ratio in the measurement of the number of photons detected during the time interval, ν_{max}^{-1} sec, and consequently ν_{max} varies as the square root of the photon flux reaching the detecting photomultiplier. In the experiments reported here this flux exceeds 10^8 photons/sec so that, for a photocathode quantum efficiency of 10%, the limiting frequency response exceeds 10 kHz.

A signal from a point on the centerline of the initial mixing region of a jet modulated at 600 Hz using the settling chamber loudspeaker is shown in Fig. 2a and it is significant that the wave form shows 100% unmixedness. The time response of the scattering system is sufficient to identify regions of 100% unmixedness at high modulation frequencies which was not possible with the gated sampling probe.[1] The stratified structure of the vortex rings which dominate the intense shear region of jet flows (shown schematically in Fig. 3) is resolved as double peaks in the signal in Fig. 2b (modulated at 900 Hz).

Finally, a typical oscillogram of scattering from a methane jet in the absence of modulation, and at a higher flowrate, is shown in Fig. 2c. Again vortex shedding is clearly apparent from the periodicity in the signal although less well-defined than previously, since the phase locking of the loudspeaker is no longer present. In order to follow fluctuations of such rapidity, Rayleigh scattering represents the only viable measuring technique.

References

[1] Grant, A. J., Jones, J. M., and Rosenfeld, J. L. J., "Orderly Structure and Unmixedness in Lifted Jet Diffusion Flames," *Combustion Institute European Symposium*, Academic Press, London, 1973, p. 548.

[2] Patankar, S. V. and Spalding, D. B., *Heat and Mass Transfer in Boundary Layers*, 2nd ed., Intertext, London, 1970, p. 158.

[3] Van De Hulst, H. C., *Light Scattering by Small Particles*, Wiley, New York, 1957.

Prediction of Yawing Force at High Angle of Attack

ANDREW B. WARDLAW JR.*

Naval Ordnance Laboratory, Silver Spring, Md.

Nomenclature

C_N = normal force coefficient = Normal Force/$q_\infty \pi r^2$
C_y = yaw force coefficient = Yaw Force/$q_\infty \pi r^2$
D = diameter of body of revolution
k = number of vortices in the flow
j = pertaining to the jth vortex
M = freestream Mach number
q_∞ = freestream dynamic pressure
r = radius of body of revolution
r_0 = reference radius
t = time
U = freestream velocity
w = dimensionless crossflow plane velocity = $(\overline{d\phi}/d\zeta)/U \sin\alpha$
w_j = dimensionless crossflow plane velocity at the location of the jth vortex. The influence of the jth vortex is neglected
x, y, z = Cartesian coordinates (see Fig. 1)
α = angle of attack
Γ = vortex circulation
ζ = complex crossflow plane coordinate = $y+iz$
ζ_{0_1}, ζ_{0_2} = crossflow plane separation points (see Fig. 1)
$\theta_{0_1}, \theta_{0_2}$ = crossflow plane separation angles (see Fig. 1)
ρ = density
λ = dimensionless circulation = $\Gamma/2\pi r U \sin\alpha$
ϕ = crossflow velocity potential
ϕ_N = nose roll angle

Introduction

At high angles of attack the leeward flowfield about a body of revolution separates and rolls up to form vortices. For relatively small angles, two symmetric vortices are formed. At larger angles, wake vortices grow unsymmetrically and are shed from the leeward side, as illustrated in Fig. 1. The resulting flowfield asymmetries induce a yawing force and moment. Simple engineering calculations can be used to determine normal forces and moments,[1-3] but a more detailed flow description must be employed if yaw forces are to be predicted.

In this Note, an approximate flowfield description is developed which is an extension of the model originally proposed by Bryson[4] and modified by Schindel.[5] The current formulation is applicable to bodies of revolution and models the flow using the impulsive flow analogy with viscous effects being simulated using point vortices. The symmetric wake assumption present in preceding studies is relaxed and growing vortices near the missile, as well as those shed into the wake, are taken into the account.

Problem Formulation

The velocity potential in the crossflow plane is formed by superimposing point vortex potentials on the potential function for flow over a cylinder. An additional source term is included to account for the changing body radius

$$\phi(\zeta) = U \sin\alpha \left\{ -\left(\zeta - \frac{r^2}{\zeta}\right) i - ir \sum_{j=1}^{k} \lambda_j \ln\left[\frac{(\zeta-\zeta_j)}{[\zeta-(r^2/\zeta_j)]}\right] + \frac{r}{\tan\alpha}\frac{dr}{dx}\ln(\zeta) \right\} \quad (1)$$

The motion of vortices in the crossflow plane is assumed to be determined by balancing the lift force on each vortex $[-i\rho\Gamma(d\zeta/dt - w_j U \sin\alpha)]$ with the force on its feeding sheet

Received November 26, 1973; revision received March 27, 1974.

Index categories: Jets, Wakes, and Viscid-Inviscid Flow Interactions; Viscous Nonboundary-Layer Flows.

* Aerospace Engineer, Applied Aerodynamics Division.

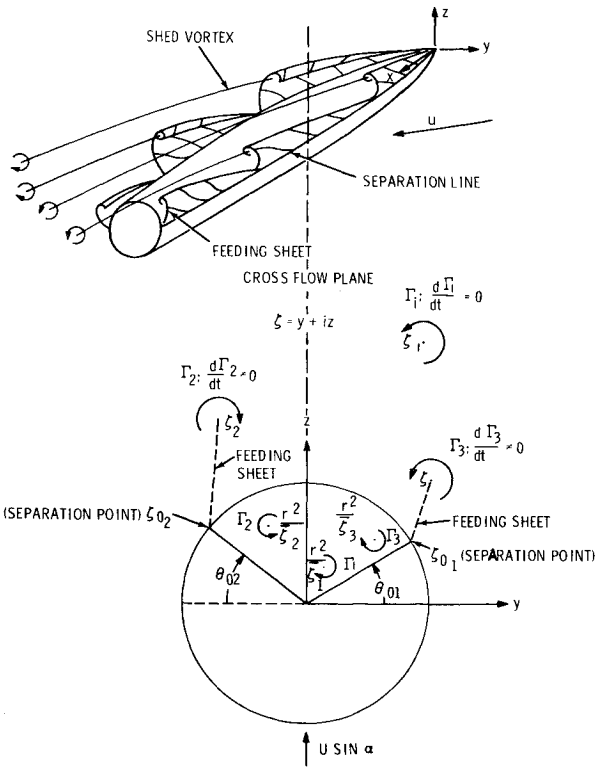

Fig. 1 Crossflow plane representation of the vortex shedding pattern of a missile at high angle of attack.

$[i\rho(\zeta_j-\zeta_{0_j})d\Gamma/dt]$. Using the relation $x = U\cos\alpha t$, the governing equations for growing vortices ($d\Gamma/dt \neq 0$) become

$$\frac{d\zeta_j}{dx} + \frac{(\zeta_j-\zeta_{0_j})}{\lambda_j}\frac{d\lambda_j}{dx} = \tan\alpha w_j - \frac{(\zeta_j-\zeta_{0_j})}{r}\frac{dr}{dx} \tag{2}$$

For vortices of constant strength, or shed vortices, the above equation reduces to

$$d\zeta_j/dx = \tan\alpha w_j \tag{3}$$

This indicates that shed vortices move with the local fluid velocity.

The circulation of growing vortices is determined by requiring that the fluid velocity at each separation point be zero

$$w_1(\zeta_{0_1}) = r(dr/dz)/(\tan\alpha\bar{\zeta}_{0_1}); \quad w_2(\zeta_{0_2}) = r(dr/dz)/(\tan\alpha\bar{\zeta}_{0_2}) \tag{4}$$

This condition uniquely determines the strength of two vortices.

Left undetermined by this formulation are the separation points in the crossflow plane and the boundary condition accompanying vortex introduction and shedding. These conditions are satisfied by introducing two vortices near the nose of the model. The x location at which these vortices are introduced is determined by: $\frac{2}{3}\tan\alpha/\sin\theta_{0_1} = dr/dx$.[4] At increasing angle of attack, this point moves past the nose of the model and vortices are introduced at the model nose. The crossflow plane locations of the vortices are taken to be along the directions $\theta_{0_1}+\pi/3$ and $\theta_{0_1}-\pi/3$ from their respective separation points, the actual distances being free parameters. Vortices are initially placed in a slightly asymmetric pattern. As the numerical solution to the governing equations progresses, asymmetry in the solution grows. When the difference in radial location of the two vortices reaches a specified value, the outermost vortex is shed and a new vortex is introduced on the same side of the body. The new vortex is assumed to lie along the sheet that previously had joined the shed vortex to the body requiring only specification of the distance from the separation point to the nascent vortex. Subsequent vortices are shed at intervals dictated by the Strouhal frequency. Initial conditions for the introduction of succeeding vortices are identical to those just described.

Application of this method requires the specification of the free parameters mentioned above. Of these, separation angle and the Strouhal number are directly measurable. Application of the measured separation angle, which is smaller than that used in the computations, leads to an erratic wake which does not resemble a vortex street. This discrepancy can be attributed to the absence of vorticity in the feeding sheet of the current model. The final set of parameters used is given in Ref. 6 and is made slightly Mach number dependent to best represent the experimental data.

Once vortex positions and strengths have been determined in the crossflow plane, the forces on a section of a model can be calculated using[7]

$$C_N + iC_Y = 2\sin\alpha\cos\alpha\left(\frac{r}{r_0}\right)^2\left[1 + \sum_{j=1}^{k}\lambda_j\left\{\frac{\zeta_j}{r} - \frac{r}{\bar{\zeta}_j}\right\}\right] \tag{5}$$

Comparison with Experiment

Experimental force measurements were made using strain gages, and schlieren pictures were obtained on a tangent ogive for $0° < \alpha < 70°$ and $0.5 < M < 1.1$. The model's over-all fineness ratio was 12 and the nose-fineness ratio was 4.0. The boundary layer was assumed to be laminar over the entire model.

The predicted normal force coefficient, as shown in Fig. 2, agrees well with the experimental data for $\alpha < 50$. The calculated center of pressure is consistently to the rear of the measured one, the difference being on the order of a caliber. A comparison between the calculated and measured yaw force coefficients at Mach 0.5 is shown in Fig. 3. In this figure, four

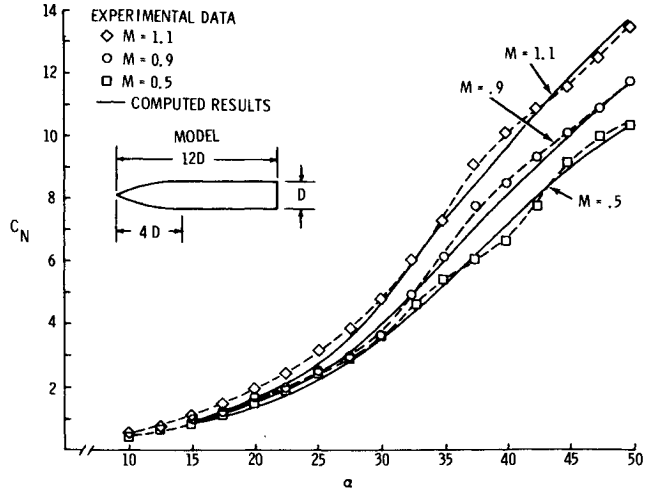

Fig. 2 Normal force coefficient as a function of angle of attack. Computed curves are based on a set of parameter values which are Mach-number dependent.

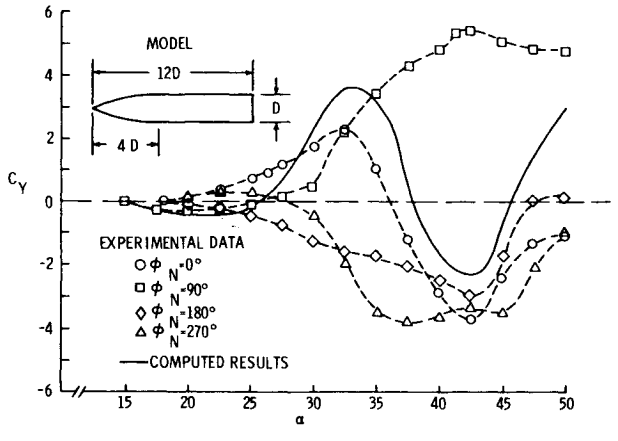

Fig. 3 Yaw force coefficient as a function of angle of attack for $M = 0.5$. Computed curve based on free parameter values which are Mach-number dependent.

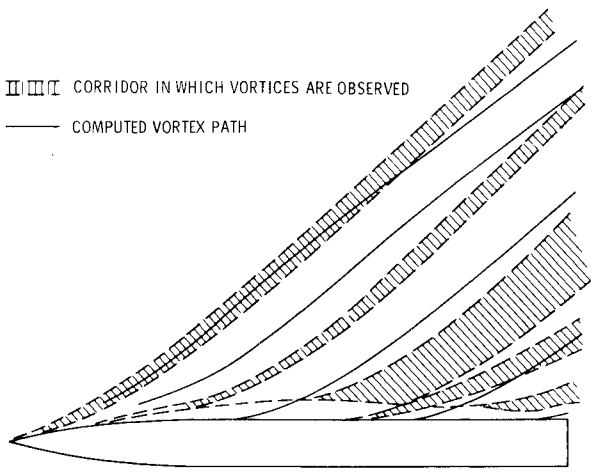

Fig. 4 Comparison of observed and computed vortex paths. $\alpha = 45°$; $M = 0.5$.

different experimental curves are shown, each corresponding to a different nose roll angle. The calculated side forces are of the correct size and occur at the appropriate range in angle of attack. For Mach numbers greater than 0.9, the side force is observed experimentally to decrease, while the predicted value of the side force remains unchanged. In Fig. 4, the predicted vortex paths are compared to those observed from schlieren pictures indicating a qualitative agreement between the predicted and observed structure of the vortex wake.

The vortex strengths predicted by the current model in the above example are typically 30% larger than those measured by Thomson and Morrison.[8]

Comparison with data obtained by G. Pick[9] indicates that the computed normal force coefficients correctly reflect the experimentally determined changes in the normal force caused by the nose bluntness, with the most satisfactory results occurring at subsonic Mach numbers. However, the decreasing yaw force coefficient which is seen to accompany increasing nose bluntness is not predicted by the current model. A more comprehensive comparison between the described model and experimental results is given in Ref. 6.

Conclusions

The model described correctly predicts normal forces and gives a good approximation of yawing forces on slender bodies at subsonic Mach numbers. For these conditions, a more accurate determination of the side forces would require an analysis which includes model and flowfield nonuniformities, since, as can be seen from Fig. 3, these parameters have a great effect on yawing force. The current model could be most improved by extending the Mach number range over which it is valid and by improving its ability to account for the effect of nose bluntness in predicting yaw forces.

References

[1] Jorgensen, L. H., "Prediction of Static Aerodynamic Characteristics for Space-Shuttle-Like and Other Bodies at Angles of Attack Varying from 0° to 180°," TN D-6996, Jan. 1973, NASA.

[2] Allen, H. J., "Estimation of Forces and Moments on Inclined Bodies of Revolution of High Fineness Ratio," RM A9126, 1949, NACA.

[3] Kelly, H. R., "Estimation of Normal Force and Pitching Moment Coefficient for Blunt Based Bodies of Revolution at Large Angles of Attack," *Journal of the Aerospace Sciences*, Vol. 21, No. 8, Aug. 1954.

[4] Bryson, A. E., "Symmetric Vortex Separation on Circular Cylinders and Cones," *Journal of Applied Mechanics*, Vol. 26, No. 4, Dec. 1959, pp. 643–648.

[5] Schindel, L. H., "Effects of Vortex Separation on the Lift Distribution of Bodies of Elliptical Cross Section," *Journal of Aircraft*, Vol. 6, No. 6, June 1969, pp. 537–542.

[6] Wardlaw, A. B., Jr., "Prediction of Normal Force, Pitching Moment, and Yawing Force on Bodies of Revolution at Angles of Attack up to 50 Degrees Using a Concentrated Vortex Flow-Field Model," NOLTR 73-209, Oct. 1973, Naval Ordnance Lab., Silver Spring, Md.

[7] Schindel, L. H., "Effects of Vortex Separation on Lifting Bodies of Elliptic Cross Section," TR 118, Sept. 1965, MIT Aerophysics Lab., Cambridge, Mass.

[8] Thomson, K. D. and Morrison, D. F., "The Spacing, Position and Strengths of Vortices in the Wake of Slender Cylindrical Bodies at Large Incidence," *Journal of Fluid Mechanics*, Vol. 50, Pt. 4, 1971, pp. 751–783.

[9] Pick, G., "Side Forces on Ogive-Cylinder Bodies at High Angles of Attack in Transonic Flow," *Journal of Spacecraft and Rockets*, Vol. 9, No. 6, June 1972, pp. 389–390.

Radiation-Gas Dynamic Shock Layer Coupling

CARL D. ENGEL* AND RICHARD C. FARMER†
Louisiana State University, Baton Rouge, La.

Nomenclature

E_2 = exponential integral
P_δ = postshock pressure
U_∞ = freestream velocity
q_R = surface radiative heat flux
$q_{R,I}$ = isothermal shock layer flux for postshock conditions
Γ = radiative cooling parameter $\Gamma = 2q_{R,I}(\frac{1}{2}\rho_\infty U_\infty{}^3)$
Δ = ratio of radiationless shock detachment distance to nose radius
δ = ratio of shock detachment distance to nose radius
$\bar{\rho}$ = density ratio across shock ρ_∞/ρ_δ

Subscripts

δ = postshock
∞ = freestream

Introduction

THE effects of radiation losses on the shock layer during hypersonic flight has been of interest for several years. Early work was characterized by examination of limiting solutions of the thin shock layer equations for optically thin and thick radiating gases to provide an overview of radiation-gas dynamic coupling.[1] More recent work has concentrated on obtaining detailed shock layer solutions which include the effects of nongray continuum and line radiation, viscous dissipation and ablation.[2–5] These detailed solutions were obtained for a variety of specific flight conditions. The purpose herein is to present detailed stagnation line shock layer results for a wide range of flight conditions which can be compared with the earlier work and provide a new overview of radiation-gas dynamic coupling within a shock layer. Only nonablating bodies are considered in this Note.

The stagnation region of a viscous radiating shock layer was modeled in Ref. 5 and is the basis for the results presented herein. This model consist of the viscous stagnation line

Received December 3, 1973. The authors are grateful for support from NASA Grant NGR 19-001-059 during the course of this investigation.

Index categories: Radiatively Coupled Flows and Heat Transfer; Supersonic and Hypersonic Flow; Radiation and Radiative Heat Transfer.

* Research Associate, Chemical Engineering Department; now Research Specialist, REMTECH Inc., Huntsville, Ala. Associate Member AIAA.

† Professor of Chemical Engineering.